



Laser-fabricated channeled Cu₆Sn₅/Sn as electrocatalyst and gas diffusion electrode for efficient CO₂ electroreduction to formate

Yijie Wang^a, Yuke Chen^a, Yiwei Zhao^{a,b}, Jiayuan Yu^a, Zhen Liu^a, Yujie Shi^a, Hong Liu^{a,b}, Xiao Li^{*,a}, Weijia Zhou^{*,a}

^a Collaborative Innovation Center of Technology and Equipment for Biological Diagnosis and Therapy in Universities of Shandong, Institute for Advanced Interdisciplinary Research (iAIR), University of Jinan, Jinan 250022, PR China

^b State Key Laboratory of Crystal Materials, Shandong University, Jinan 250100, PR China

ARTICLE INFO

Keywords:
CO₂ electroreduction
Laser irradiation
Gas diffusion electrode
Electric field distribution
Formate

ABSTRACT

Formate synthesis by CO₂ electroreduction reaction (CO₂RR) has been considered as a promising strategy for mitigating the excessive CO₂. Here, we synthesize Cu₆Sn₅ alloy on Sn foil (Cu₆Sn₅/Sn) and gas diffusion electrode (GDE) using laser irradiation. Cu₆Sn₅/Sn exhibits high formate faradaic efficiency (FE_{formate}) of 87.2% and remains stable at 28.69 mA cm⁻² over 14 h. Further, with the help of laser drilling, the channeled Cu₆Sn₅/Sn used directly as GDE shows increased current density (118 mA cm⁻²) and steady FE_{formate} (86.69%) in flow cell. Density functional theory (DFT) calculations reveal that the high performance of Cu₆Sn₅/Sn benefits from the appropriate binding energy of the key intermediates *OCHO. Meanwhile, COMSOL simulation results of CO₂ concentration and electric field distribution combined with the results of kelvin probe force microscopy (KPFM) prove that CO₂RR prefers to occur around the channels of electrode. More importantly, this laser irradiation method is also available to synthesize other alloy electrocatalysts.

1. Introduction

The emission of greenhouse gases had exceeded the digestive capacity of the earth, causing environmental and economic losses and ocean acidification [1]. CO₂ electroreduction reaction (CO₂RR) which could convert CO₂ into fuels and chemicals was a promising method for solving this problem, because it could be powered by sustainable energy like solar or wind energy to product C-based fuels at ambient temperatures and pressures [2]. However, CO₂RR still had problems of low reduction efficiency and poor product selectivity. Compared to theoretical potentials required to form target products (Table S1), the more negative potential was required to overcome the energy barriers within the multiple-step protons/electrons reactions of CO₂RR [3]. To overcome these problems, extensive efforts had been devoted to synthesize electrocatalyst which had high CO₂RR current density and high product selectivity, such as single metals [4], metal oxides [5], and nitrides [6] et al. Among many kinds of metals, Sn had emerged as an interesting metal for its low-cost, environmentally friendly and high selectivity towards high-valuable formate [7]. Further, in order to achieve high current density and selectivity, many studies had focused on the

introduction of metal heteroatoms into Sn to form alloy, such as Cu [8], Pd [9], Pb [10], Bi [11], etc. Among these metals, Cu had the advantages of low cost and strong electrical conductivity, and also showed significant formate selectivity at low overpotentials [12]. The combination of Sn and Cu effectively met the demand to improve the selectivity and stability of CO₂RR [13]. Alloy catalysts had been prepared by various methods, such as electrodeposition [14], solvent reduction [15] and galvanic replacement [16]. For instance, Chen et al. synthesized Cu-Sn electrocatalyst (Cu₃Sn/Cu₆Sn₅) using electrodeposition process following thermal annealing and achieved the faradic efficiency of formate (FE_{formate}) of 82% and a current density of 18.9 mA cm⁻² at -1.0 V vs. RHE for 42 h [17]. With higher requirements of uniform and controllable composition, the more efficient and convenient methods needed to be developed to construct alloy electrodes for CO₂RR. In addition, except for preparing high-efficient catalysts, the construction of gas diffusion electrode (GDE) was also an important way to improve the current density of CO₂RR. Commercial demand was estimated to require over 100 mA cm⁻² [18], however, traditional H-cell configuration had disadvantage of hardly achieving high current density because of the solubility limit of CO₂ and low CO₂ diffusion [19]. In order to

* Corresponding authors.

E-mail addresses: ifc_lix@ujn.edu.cn (X. Li), ifc_zhouwj@ujn.edu.cn (W. Zhou).



solve these problems, GDE and flow-cell configuration were brought into use. Traditional GDE composed of gas diffusion layer (GDL) and catalyst with adhesives, where the GDL continuously feed CO_2 to the catalyst surface and enhancing the gas transport to the electrochemical interface [20]. When electrocatalysts were supported in the GDL, a three-phase interface, including electrolyte (liquid), catalyst (solid) and CO_2 (gas) was formed, where CO_2RR occurred [21]. Benefitted by overcoming the limit of mass-transport, the catalytic performance in the flow-cell had been greatly improved. For example, Sargent et al. reported microporous Cu GDE achieved the FE_{ethylene} of 70% and a current density of 275 mA cm^{-2} at super alkaline electrolyte (10 M KOH) [22]. In conclusion, the preparation of Sn-based alloy catalysts and the construction of GDE could effectively improve the efficiency of CO_2RR .

Recently, laser irradiation had been adopted as a facile one-step synthesis technique to directly synthesize catalysts for various applications [23,24]. Firstly, the capacity of controlling the position of energy delivery and duration of heating made nanosecond pulsed laser irradiation a well-established technique for synthesizing nanoparticles [25]. For example, Li et al. used laser irradiation induced alloying and subsequently chemical etching method prepared highly active AuAgPt alloy catalyst for electrooxidation. The superb electrocatalytic activity was attributed to the alloying process during laser irradiation. During the fast fusion process, amounts of grain boundaries and hierarchical structures were produced, farther promoting the activity performance [26]. Secondly, ultraviolet (UV) laser could directly destroy the chemical bonds of the material without thermal deformation due to the small beam spot size (with the diameter of 0.7 mm). Considering these strengths, UV laser had potentials in the preparation of micro-nano structures, such as nanoparticles, micro-grooves [27,28].

In this work, we demonstrated a simple one-pot fabrication of $\text{Cu}_6\text{Sn}_5/\text{Sn}$ by nanosecond pulsed UV laser irradiation. Remarkably, Cu_6Sn_5 alloy was showed high selectivity for CO_2RR to formate, with a high FE_{formate} (87.2%) and current density of 28.69 mA cm^{-2} in a CO_2 -saturated 0.5 M NaHCO_3 electrolyte solution at -0.95 V vs. RHE. Further, the obtained porous $\text{Cu}_6\text{Sn}_5/\text{Sn}$ were directly used as catalyst and GDE in a commercial flow-cell electrolyzer, showing the increased current density and high FE_{formate} (118 mA cm^{-2} and 86.69% at -1.0 V vs. RHE). The theoretical calculations were used to investigate the catalytic sites of $\text{Cu}_6\text{Sn}_5/\text{Sn}$, the electric field distribution and CO_2 gas diffusion kinetics of GDE.

2. Experimental methods

2.1. Chemicals

Sn foils (99.99%), Cu foils (99.99%), Mo foils (99.99%), Ni foils (99.99%) and Ag foils (99.99%) were purchased from Dahe New Energy Co., Ltd. Ethanol absolute ($\text{C}_2\text{H}_5\text{OH}$), hydrochloric acid (HCl), sodium bicarbonate (NaHCO_3) and potassium hydroxide (KOH) were purchased from Sinopharm Chemical Reagent Co., Ltd. CO_2 (purity 99.99%) and Ar (purity 99.99%) were obtained from Jining Gases (Shandong, China). Unless otherwise stated, all reagents were used without further purification. Deionized (DI) water was supplied by Barnstead Water System (Smart2Pure 6UV, 18.2 $\text{M}\Omega \text{ cm}$).

2.2. Preparation of Cu_6Sn_5 on Sn Foil ($\text{Cu}_6\text{Sn}_5/\text{Sn}$)

Cu_6Sn_5 catalyst was prepared by laser irradiation. First, Sn foil and Cu foil were cleaned with anhydrous ethanol and DI water for 10 min to remove organic matters and impurities on the surface. Second, Cu foil with 0.01 mm thickness on Sn foil with 0.05 mm thickness was put on the vibration reduction table of the nanosecond pulsed UV laser device (Shanghai Fermi Laser Technology Co., Ltd., Pulse 355-3) with the wavelength of 355 nm and the pulse width of 16 ns to ensure the accuracy, which was also equipped with vacuum pump to keep the metal sheets close-contact. Then, Cu foil was processed by laser scanning with

the certain power (0.72 W), which was set by the software installed on computer. In the process of scanning, the laser-treated Cu foil fused and combined with Sn foil below. The black Cu-Sn catalyst supported on Sn foil were obtained and cleaned by ultrasonic for 5 s to remove the residual powder, following dried by N_2 flow. Before determining the final sample, laser power (0.60, 0.66, 0.72, 0.78, 0.84 W) and the thickness of Cu foil (0.002, 0.01, 0.02 mm) were optimized, the results were shown in Figs. S1–S3, respectively. In addition, cleaned Cu foil and Sn foil were also processed for comparison using UV laser device with the power of 0.6 and 0.3 W, named L-Cu and L-Sn, respectively.

2.3. Preparation of porous $\text{Cu}_6\text{Sn}_5/\text{Sn}$ gas diffusion electrode ($\text{Cu}_6\text{Sn}_5/\text{Sn}$ GDE)

Cu_6Sn_5 alloy was first prepared on Sn foil using the above method. To enable CO_2 diffuse from gas compartment to cathode electrolyte and reduce the damage of alloy, the side of Sn foil that no alloy loaded was punched with laser power of 1.35 W, named $\text{Cu}_6\text{Sn}_5/\text{Sn}$ GDE. The radius size of pores was controlled in $\sim 20 \mu\text{m}$ and the pitch of pores was set in $400 \mu\text{m}$ to ensure efficient CO_2 access and reduce the likelihood of electrolyte flooding.

2.4. Preparation of other alloy catalysts and GDE

Other alloy catalysts and corresponding GDE were also synthesized through the laser irradiation method, such as Cu-Ag, Cu-Mo and Cu-Ni. The preparation processes were as follows. The stacked Cu foil with 0.01 mm thickness and other metal foil (Ag, Mo, and Ni) with 0.05 mm thickness were put on the vibration reduction table of the nanosecond pulsed UV laser device, respectively. Then, Cu foil was processed by laser scanning with the certain power (1.2 W). In the process of scanning, the laser-treated Cu foil fused and combined with metal foil below and formed alloy. Similarly, in order to prepare GDE, these alloy electrodes were punched with laser power of 2.7 W to form channels. The SEM images and XRD results of these alloy catalysts and GDE were shown in Fig. S4.

2.5. Characterization

Field emission scanning electron microscope (FESEM) and transmission electron microscopy (TEM) and high-resolution TEM (HRTEM) images were taken on a Hitachi regulus 8100 and Thermo Fischer Talos F200x to analyze morphologies and element distribution characterization of materials, respectively. X-ray diffractometer (XRD, Cu K α radiation, $\lambda = 0.15406 \text{ nm}$, Thermo Fisher, ARL Equinox 3000X) were used to measure phase composition of the as-made materials. The states of surface elements were characterized using X-ray photoelectron spectra (XPS, Shimadzu, AXIS Ultra Supra). High-speed video camera (FuHuang AgileDevice Co., Ltd, X213) was used to verify the high energy of Cu particles that were dropped by laser shock. High-resolution X-ray Tomography (Zeiss Xradia 510 Versa) was used to investigate the micro-structural of $\text{Cu}_6\text{Sn}_5/\text{Sn}$ GDE, before analysis, samples were prepared as the square with 1 mm sides. Contact Angle (CA, POWERREACH, JC2000D2G) was used to measure the wettability of samples. Atomic force microscope and kelvin probe force microscopy (AFM and KPFM, BRUKER Dimension Icon with Scan Asyst) were used to measure the surface roughness of the sample and the contact potential difference between the probe (SCM-PIT-V2) and sample.

2.6. Electrochemical measurements

All CO_2 electrochemical reduction measurements were performed with an electrochemical workstation (CHI 760E, CH Instruments Inc.) in a typical H-type two compartment glass cell separated by Nafion 211 membrane, using 0.5 M NaHCO_3 solution as electrolyte (Fig. S5). Each compartment contained 40 mL electrolyte with total volume of 100 mL.

Laser treated metal sheet acted as working electrode was used directly without any additional binder, while the untreated part was fully covered with commercial hot glue. An Hg/Hg₂Cl₂ electrode (SCE, saturated KCl) and platinum sheet were used as the reference and counter electrode, respectively. All the electrode potentials mentioned below were converted to the RHE scale using the equation as follows: E (RHE) = E (Hg/Hg₂Cl₂) + 0.242 + 0.061 × pH. Before the test of CO₂RR, CO₂ gas was constantly pumped into the cathodic compartment for 15 min to ensure the electrolyte was saturated with CO₂. During the reduction process, the catholyte was stirred at a rate of 700 rpm.

2.7. Flow cell measurements

Flow cell measurements were performed in a commercial flow cell electrolyser (101017, Gaoss Union (Wuhan) Technology Co., LTD) containing gas, cathode and anode compartment (Fig. S6). The cathode adopted porous Cu₆Sn₅/Sn as GDE and catalyst. Sn foil contacted gas compartment and Cu₆Sn₅ contacted cathode compartment, while the untreated part was fully covered with glue. A slice of proton exchange membrane (PEM, Nafion 211) with the size of 35 × 15 mm² was acted as the separator, and RuO₂-loaded hydrophobic carbon paper with the amount of load of 1 mg cm⁻² as the anode. Hg/HgO reference electrode was located inside the cathode compartment. During the reduction experiments, CO₂ was directly pumped into gas compartment at a rate of 30 sccm and through the porous Sn foil to cathode compartment, note that, the outlet of gas compartment was sealed to ensure the above action carried out. 1 M KOH was used as catholyte and continuously circulated with the help of a pump through the cathode compartment at a rate of 30 sccm.

2.8. Product analysis

After the reduction experiments, 5 mL gas containing CO₂ and gaseous products was extracted from the reactor and directly pumped into gas chromatograph (GC, Agilent GC 7890B) with a syringe for quantification of the gaseous products. For the liquid products of CO₂RR, we retained about 15 mL cathode electrolyte and adjusted the pH value to 2.5 and injected it into the high-performance liquid chromatography (LC, EClassical, R1-201 H) with a liquid injection needle. The Faradaic efficiency of products was calculated as follows: FE_{product} = n_{product} × z_{product} × F/Q, where n_{product} was the total amount of product, z_{product} was the electron transfer number needed to produce product (z_{CO} = 2, z_{formate} = 2), F was the Faraday constant, Q was the total amount of consumed charge, which could be calculated by multiplying the current density and the running time.

2.9. Density functional theory (DFT) computations

All the computations were carried out using Vienna ab initio simulation package (VASP) within the framework of density functional theory (DFT) [29,30]. The ion-electron interactions were described by the projector augmented wave method and the general gradient approximation in the Perdew–Burke–Ernzerhof form was used. A cut-off energy of 350 eV for plane-wave basis set was employed. During the structure relaxation, the convergence criterion was set to 0.03 eV Å⁻¹ and 10⁻⁵ eV for the residual force and energy, respectively. 2 × 1 × 1 α-Sn (211), 3 × 3 × 1 fcc Cu (111) and 1 × 2 × 1 Cu₆Sn₅ (22–1) slabs were used to simulated the Sn, Cu and Cu₆Sn₅, respectively. The corresponding Brillouin zones was sampled using 4 × 3 × 1, 4 × 4 × 1 and 2 × 3 × 1 Monkhorst-Pack k-mesh, respectively [31]. The detailed calculation of the k-point sampling were shown in Fig. S7. In order to avoid the interaction between two periodic units, a vacuum space of 15 Å was employed.

The Gibbs free energy change (ΔG) of each electrochemical process was calculated based on the computational hydrogen electrode (CHE) model as following [32]:

$$\Delta G = \Delta E + \Delta E_{ZPE} - T\Delta S$$

where ΔE was the reaction energy difference, E_{ZPE} was the zero-point energies, T was temperature and S was entropy. The coordinates of the model systems and the detailed results for DFT calculation were shown in Table S2.

2.10. COMSOL multiphysics simulation

For the simulation of the velocity and pressure field, a 3D model was established using Stationary Incompressible Flow over a Backstep module in COMSOL Multiphysics software. This model included five channels with a diameter of 20 μm and a diffusion layer with a size of 1 × 1 × 0.2 mm.

For the simulation of the electric field distribution, a 2D model with a size of 200 × 250 μm was established. Same as the experimental conditions, the channel diameter was set to 20 μm. The simulation satisfied the charge conversation equations: E = −∇V and ∇ × (ε₀ε_rE) = ρ_v, where E was electric field, V was potential, ε₀ was the permittivity of vacuum, ε_r was the relative dielectric constant, ρ_v was the space charge density. The initial potential was set as 0 V, the potential boundary above the model was set as 0.0225 V (approximate conversion based on the actual potential and the distance between the positive and negative electrodes), and the other boundary conditions were set as zero-charge boundary.

3. Results and discussion

3.1. Fabrication and characterization of Cu₆Sn₅/Sn

The preparation process of Cu-Sn alloy by one-step laser irradiation method was schematically showed in Fig. 1a. The Cu foil as Cu source was stacked on Sn foil as Sn source. When the high-energy UV laser photons hit the Cu foil, the high-speed Cu particles (red circle) with an acceleration of 29622 m s⁻² were produced, which hit the Sn foil to form the Cu-Sn alloy particles on the surface of Sn foil. Large-scale of carved Cu foil and Sn foil with deposited Cu-Sn alloy after laser irradiation with “CO₂” pattern with the size of 3 × 2 cm² were showed in Fig. 1b and e. The according preparation only needed 15 min at a fast laser-scan speed (200 mm s⁻¹), intuitively demonstrated the high efficiency of UV laser. The carved “CO₂” pattern was observed on Cu foil, meanwhile, the black and protruding “CO₂” pattern was observed on Sn foil. Besides, micron-scale pattern was also prepared, the FESEM image in Fig. 1c showed that Cu foil was punctured after laser-scanning with “CO₂” pattern, and the corresponding elemental mapping in Fig. 1d showed no Cu element was detected in the “CO₂” pattern. At the same time, protruded “CO₂” pattern in Fig. 1f and g showed the uniform distribution of Sn and Cu elements on “CO₂” pattern.

To illustrate the controllability of laser, the Cu-Sn alloys with different sizes (0.04–2.25 cm²) and “UJN” pattern (the size of each alloy unit was 7 × 7 mm²) were showed in Fig. 2a, which could be completed within 1–10 min at the fast laser-scanning speed (200 mm s⁻¹). The morphology of as-prepared Cu-Sn alloy was confirmed by FESEM measurements. As shown in Fig. 2b and c, it could be clearly seen that a number of villiform nanospheres with sizes of about 500 nm were uniformly covered on the surface of Sn foil. Meanwhile, the thickness of the alloy layer was confirmed to be 18.88 μm by the EDS elemental mapping of the cross section (Fig. S2). The XRD pattern (Fig. 2d) showed the diffraction peaks of Sn substrate (PDF#04–0673) at 30.64°, 32.02°, 43.87°, 44.90° and 55.33° corresponded to the (200), (101), (220), (211) and (301) planes. The main peaks at 30.09°, 42.97°, 43.27 and 53.38° were corresponded to the (22–1), (132), (42–2), and (24–1) planes of Cu₆Sn₅ (PDF#45–1488) [33], indicating that Cu₆Sn₅ alloy was successfully prepared on Sn substrate, named Cu₆Sn₅/Sn. Transmission electron microscopy (TEM) further showed the structure of as-prepared

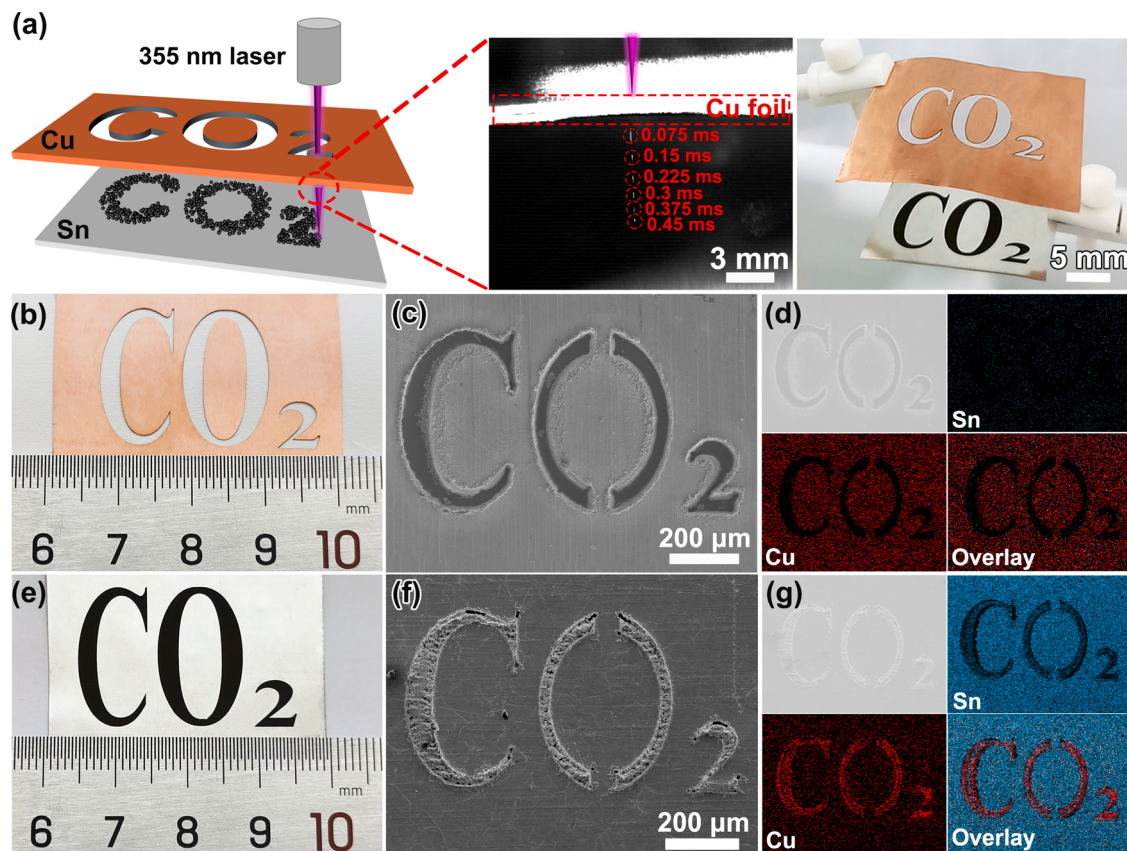


Fig. 1. (a) Synthetic scheme, high speed camera results and physical display of Cu-Sn alloy supported on Sn foil. (b and e) Large-size photographs, (c and f) micron-size FESEM and (d and g) corresponding mapping of carved Cu foil (b-d) and Sn foil with deposited Cu-Sn alloy (e-g) after laser irradiation with "CO₂" pattern.

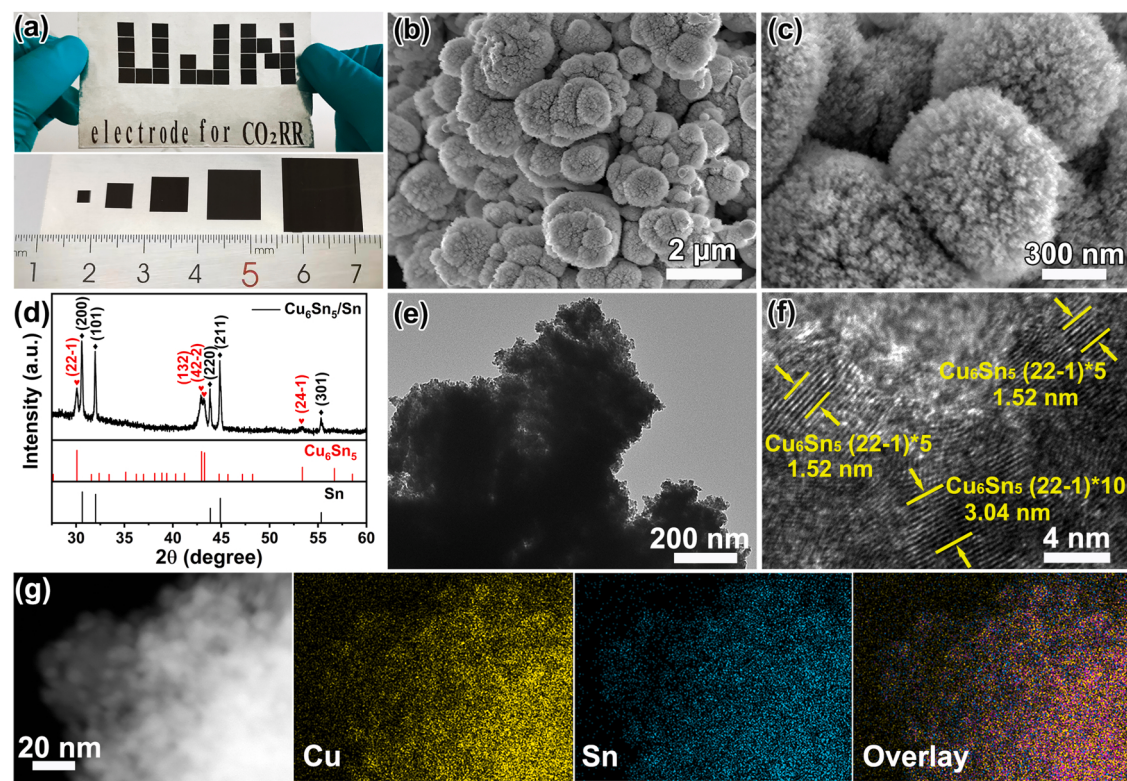


Fig. 2. (a) The "UJN" pattern composed of Cu-Sn alloy with the size of 0.7 × 0.7 cm². (b and c) FESEM images, (d) XRD pattern, (e and f) TEM images and (g) corresponding EDS elemental mapping of Cu₆Sn₅ alloy.

Cu_6Sn_5 alloy. TEM images in Fig. 2e showed that Cu_6Sn_5 were assembled by villous nanoparticles. The high-resolution TEM image (Fig. 2f) revealed that the crystal lattice spacing was estimated to be 0.304 nm, which was in accordance with the (22-1) crystal face of Cu_6Sn_5 . The corresponding energy-dispersive X-ray spectroscopy (EDS) element mapping images (Fig. 2g) indicated the homogeneous distribution of the Sn and Cu elements, implying the uniformity of the Cu_6Sn_5 alloy.

3.2. Electrochemical CO_2 reduction performance

To study the CO_2 electrocatalytic reduction of laser prepared $\text{Cu}_6\text{Sn}_5/\text{Sn}$, the blank samples of L-Cu and L-Sn were treated by laser irradiation under the same mode, respectively. FESEM images and XRD results of L-Cu and L-Sn were shown in Fig. S8. After the laser irradiation, the roughness of Cu foil and Sn foil increased, covered with numerous nanoparticles. XRD results showed the laser treatment did not change the phase of the sheet metals, remained as Cu and Sn phase. For electroreduction test, the as-prepared $\text{Cu}_6\text{Sn}_5/\text{Sn}$, L-Sn and L-Cu electrodes were tested in the typical H-type cell filled with 0.5 M NaHCO_3 . It was worth noting that the laser-untreated region of electrode was fully covered with commercial hot glue to avoid the influence of substrate on electrochemical performance. The cathodic polarization curves of three prepared electrodes were tested ranged from 0 to -1.1 V vs. RHE in Ar and CO_2 saturated 0.5 M NaHCO_3 electrolytes, respectively. As shown in Fig. 3a, dashed lines were used to represent their performance in Ar saturated electrolyte. Because of the chemical stability of Ar, reactions occurred in this range were corresponding to hydrogen evolution reaction (HER). Obviously, compared with L-Cu, $\text{Cu}_6\text{Sn}_5/\text{Sn}$ and L-Sn exhibited lower current densities under the same conditions, indicating the inactivation of HER. When CO_2 was saturated in the electrolyte, different from L-Sn and L-Cu, the current density of $\text{Cu}_6\text{Sn}_5/\text{Sn}$ increased sharply, suggesting that $\text{Cu}_6\text{Sn}_5/\text{Sn}$ were likely more conductive to electrochemical CO_2 reduction. Therefore, the chronoamperometric responses in CO_2 -saturated electrolyte and the FE for H_2 , CO, and formate of $\text{Cu}_6\text{Sn}_5/\text{Sn}$ at different potentials were shown in Figs. S9 and 3b. The chronoamperometric responses were stable and $\text{FE}_{\text{formate}}$ showed a volcano shape at the range from -0.75 to -1.15 V vs. RHE. It was worth noting that the $\text{FE}_{\text{formate}}$ kept steady above 80% from -0.85

to -1.05 V vs. RHE and attained a maximum value of 87.2% at -0.95 V vs. RHE. At the same time, the FE_{H_2} remained at around 7%, proving that $\text{Cu}_6\text{Sn}_5/\text{Sn}$ catalyst had the ability to maintain a stable CO_2RR activity and suppress HER in a wide voltage range. The sum of FE for all reduction products were approximate 100%, indicating that no significant amounts of other reduction products were formed in the experiment. $\text{FE}_{\text{formate}}$ of $\text{Cu}_6\text{Sn}_5/\text{Sn}$ was compared with other Sn-based catalysts reported in recent years, as shown in Table S3, suggesting $\text{Cu}_6\text{Sn}_5/\text{Sn}$ exhibited superior selectivity. The partial current densities for three reduction products were shown in Fig. 3c. $\text{Cu}_6\text{Sn}_5/\text{Sn}$ electrode showed low current densities for H_2 and CO while formate had a much higher current density. As the voltage increased, the current density of formate increased at a faster rate. When the applied voltage kept to increase, the growth rate of formate slowed down and the current density of H_2 showed a trend of increase, indicating the suppression for HER started to weaken, which was correspond to the growth of FE_{H_2} .

Owing to the acceleration of electron transfer rate [34], alloy catalysts might have better catalytic performance than pure metal. To confirm this statement, the FE for the $\text{Cu}_6\text{Sn}_5/\text{Sn}$, L-Sn and L-Cu (Fig. 3d and S10) were compared. The L-Cu showed trace formate production and low CO production ($\text{FE}_{\text{CO}} < 10\%$), while primary production was H_2 ($\text{FE}_{\text{H}_2} > 40\%$). The $\text{FE}_{\text{formate}}$ for L-Sn and $\text{Cu}_6\text{Sn}_5/\text{Sn}$ increased obviously while that of H_2 and CO decreased, proving that the existence of Sn could promote the conversion efficiency of CO_2 into formate and depressed the H_2 and CO production at the potential from -0.85 to -1.05 V vs. RHE. Like $\text{Cu}_6\text{Sn}_5/\text{Sn}$, the formate selectivity of L-Sn showed a typical volcano shape, reaching a maximum $\text{FE}_{\text{formate}}$ value of 58%, while $\text{Cu}_6\text{Sn}_5/\text{Sn}$ showed a much higher $\text{FE}_{\text{formate}}$, suggesting the formation of alloy greatly improved the selectivity of catalyst for formate. Besides the high efficiency, this laser method allowed Cu-Sn alloy to directly grow on Sn substrate, which could accelerate the electron transfer between the active sites and CO_2 , and avoided the use of binding materials, making the material could expose more active sites [35]. As shown in Fig. S11, compared with those of L-Cu and L-Sn, the smaller charge transfer resistance (Rct , $27\ \Omega$) of $\text{Cu}_6\text{Sn}_5/\text{Sn}$ suggested faster charge-transfer speed between electrode and electrolyte [36–38]. Taken together, these results demonstrated that the CO_2RR performance could be dramatically improved after forming Cu_6Sn_5 alloy on Sn foil by laser

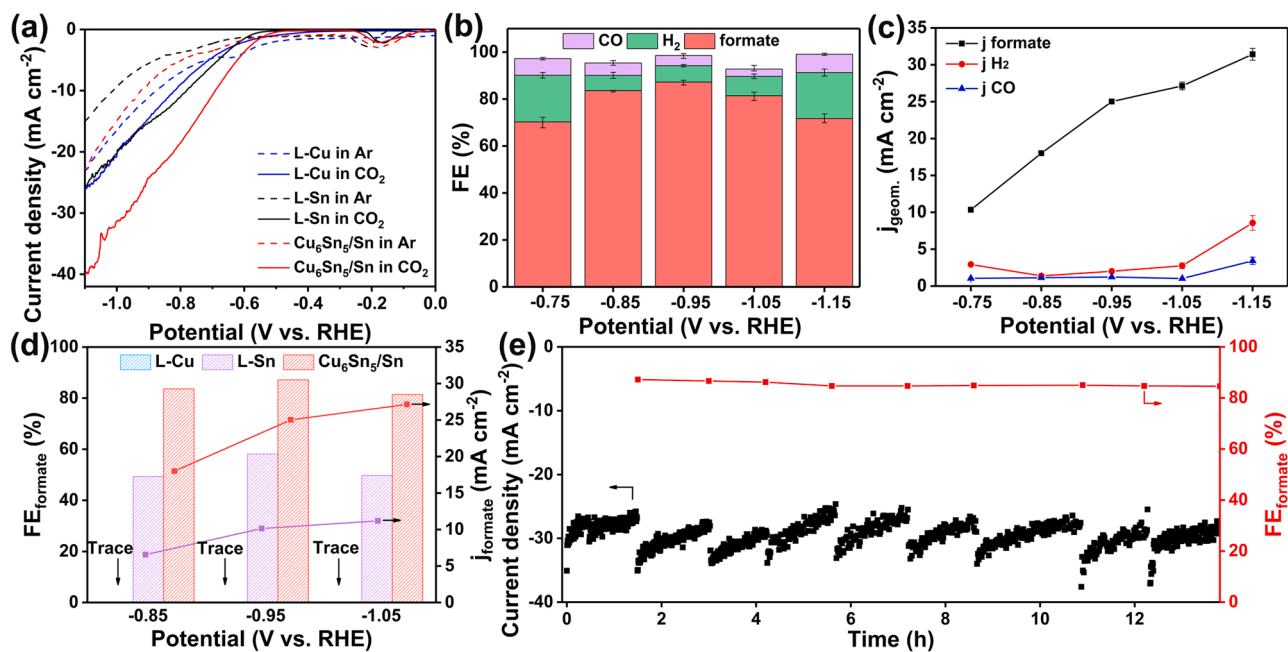


Fig. 3. (a) Polarization curves of $\text{Cu}_6\text{Sn}_5/\text{Sn}$, L-Sn and L-Cu catalysts in Ar and CO_2 saturated 0.5 M NaHCO_3 electrolyte with scan rate of $5\ \text{mV s}^{-1}$. (b) FEs and (c) partial current densities of H_2 , CO and formate for $\text{Cu}_6\text{Sn}_5/\text{Sn}$ electrode normalized by geometric area. (d) $\text{FE}_{\text{formate}}$ over $\text{Cu}_6\text{Sn}_5/\text{Sn}$, L-Sn and L-Cu electrode. (e) Long-term stability and $\text{FE}_{\text{formate}}$ curve of $\text{Cu}_6\text{Sn}_5/\text{Sn}$ catalyst for 14 h at -0.95 V vs. RHE.

irradiation.

To further assess the electrochemical stability of $\text{Cu}_6\text{Sn}_5/\text{Sn}$ catalyst, the long-term durability was examined under the optimal overpotential at -0.95 V vs. RHE (Fig. 3e). The catalyst during continuous test for 14 h exhibited almost invariant current density and $\text{FE}_{\text{formate}}$, meaning that $\text{Cu}_6\text{Sn}_5/\text{Sn}$ maintained a stable activity during the long-term test. There were no evident changes occurred in the LSV curves, XRD and FESEM image after long-term test (Fig. S12), these also showed the excellent catalytic and structural stability of $\text{Cu}_6\text{Sn}_5/\text{Sn}$ catalyst.

3.3. Theoretical analysis to CO_2RR performance on $\text{Cu}_6\text{Sn}_5/\text{Sn}$

Above electroreduction results established the outstanding selectivity and remarkable long-term stability of $\text{Cu}_6\text{Sn}_5/\text{Sn}$ catalyst, which was owing to the alloying of two metals. For the purpose of gaining more insights into the probable influence of the alloying on the CO_2RR selectivity, X-ray photoelectron spectroscopy (XPS) analysis and DFT calculations were carried out. From the XPS results in Fig. 4a and b, the Cu 2p doublet of Cu_6Sn_5 was shifted by 0.195 eV toward lower binding energy relative to that of L-Cu. While the binding energy of Sn^0 (484.7 and 493.1 eV) for Cu_6Sn_5 alloy positively shifted compared to L-Sn (484.5 and 492.9 eV). These results indicated that charges were transferred from Sn to Cu [39–41], and the decreased number of electrons happened on Sn after the alloying caused the reduction of Fermi level on the valence band of 3d orbit, which would facilitate the chemically adsorbed of CO_2 and thus accelerate the CO_2RR [15,42].

Furthermore, DFT calculations were performed to simulate and contrast the CO_2RR ability on Sn (211), Cu (111) and Cu_6Sn_5 (22–1), respectively. All the computations were performed by using Vienna ab

initio simulation package (VASP) [29,30]. The ion-electron interactions were described by the projector augmented wave method [31] and the general gradient approximation in the Perdew-Burke-Ernzerhof (PBE) form was used [43,44]. Net Bader charges analysis was conducted to study the charge distribution after the alloying of Sn with Cu. As showed in Fig. 4c, Sn was positively charged in the Cu_6Sn_5 , indicated that Sn would donate charge to Cu, which was consistent with XPS results. As proved by the previous study [45], the positive charged Sn sites would increase the thermodynamic barrier to $^*\text{COOH}$, and thus the pathway through the $^*\text{OCHO}$ intermediate was likely preferred over the $^*\text{COOH}$ intermediate for the formate production. Therefore, the free energy diagrams on Cu, Sn and Cu_6Sn_5 were constructed. The α -phase for Sn, a face-centred cubic (fcc) structure for Cu and the slab structure for Cu_6Sn_5 were used (Fig. 4d). The structures of the intermediates ($^*\text{OCHO}$, $^*\text{COOH}$, $^*\text{CO}$ and H^*) were shown in Fig. S13. Note that Cu_6Sn_5 alloy were divided into two adsorption sites (Cu and Sn) to figure out the true active site. According to previous studies, when the limiting potential was determined by the step of $^*\text{OCHO}$ hydrogenation, the reaction preferred to generating formate. Relatively, when the limiting potential step was the formation of $^*\text{COOH}$, CO was easier to generate [46]. Although $^*\text{COOH}$ was also been regarded as the intermediate for formate production, the thermodynamic and chemisorption energies limitation suggested that $^*\text{OCHO}$ was the key intermediate for the CO_2RR to formate [33,47,48]. As shown in Fig. 4e and f, after the alloying of Cu and Sn, when Sn acted as active site ($\text{Cu}_6\text{Sn}_5\text{-Sn}$), the binding energy of intermediates $^*\text{OCHO}$ (0 eV) was much more moderate than those of $^*\text{OCHO}$ on Cu (-0.15 eV), Sn (-0.11 eV) and $\text{Cu}_6\text{Sn}_5\text{-Cu}$ (-0.37 eV), suggesting that the generation of formate was more preferred on $\text{Cu}_6\text{Sn}_5\text{-Sn}$. Alternately, when Cu acted as active site,

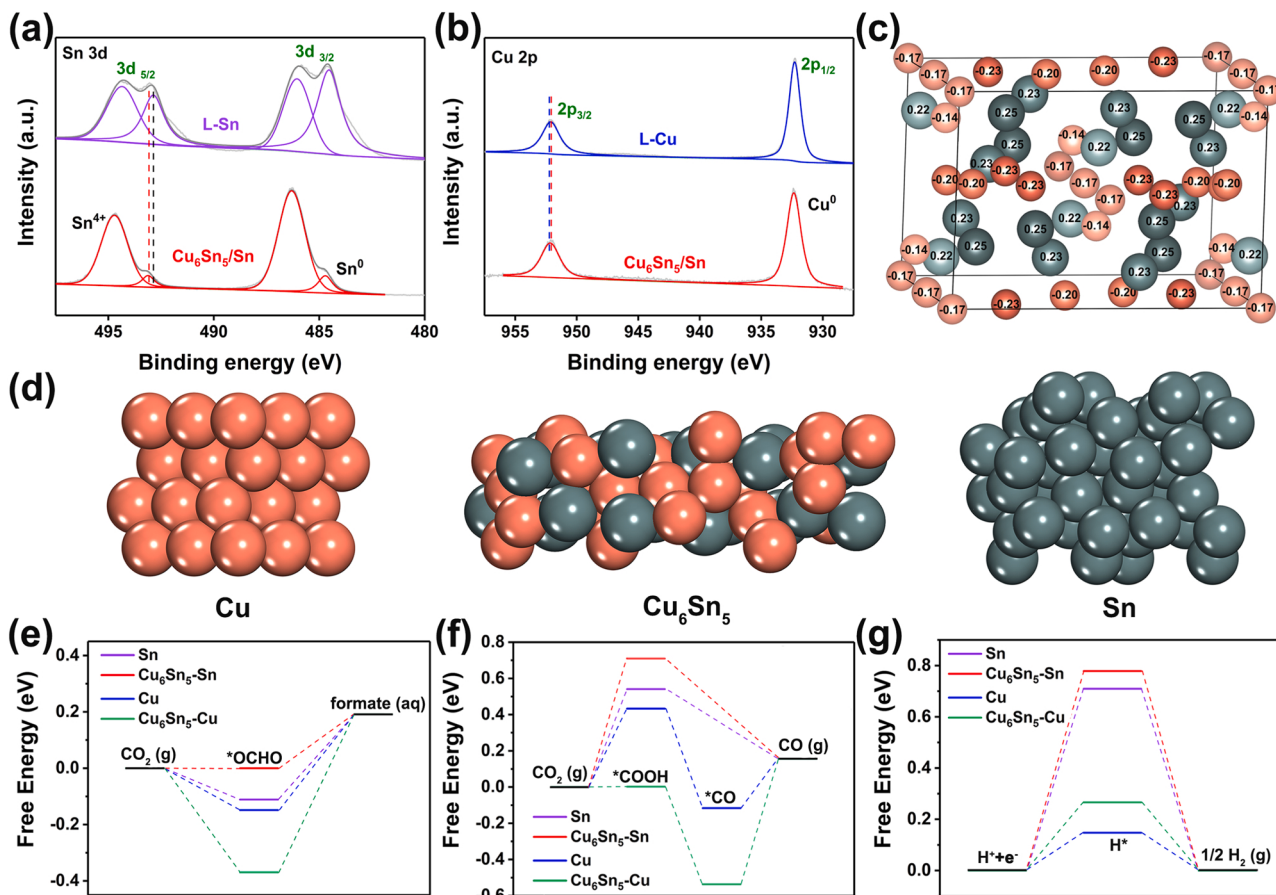


Fig. 4. (a) Sn 3d XPS spectrum of L-Sn and $\text{Cu}_6\text{Sn}_5/\text{Sn}$. (b) Cu 2p XPS spectrum of $\text{Cu}_6\text{Sn}_5/\text{Sn}$ and L-Cu. (c) Net Bader charges of the atoms in the Cu_6Sn_5 unit cell. A positive value indicates the atom to be positively charged. (d) Optimized structures of pure Sn, Cu_6Sn_5 , and Cu (see Fig. S13 for the configurations with absorbed intermediates). Free Energy for (e) formate, (f) CO and (g) H_2 on Sn, $\text{Cu}_6\text{Sn}_5\text{-Sn}$, $\text{Cu}_6\text{Sn}_5\text{-Cu}$ and Cu, respectively.

the binding of intermediates $^*\text{COOH}$ was optimal. Combining the experimental and calculated results, we could conclude that Sn was the main active site in the prepared alloy. Besides, the Gibbs free energy diagram for HER process (Fig. 4g) revealing that $\text{Cu}_6\text{Sn}_5\text{-Sn}$ showed the superior inhibition of HER over pure metals and $\text{Cu}_6\text{Sn}_5\text{-Cu}$ through weakening the binding of the intermediate H^* [49], which was also consistent with the experimental results. In general, the results of XPS and DFT calculations suggested that Sn in Cu_6Sn_5 was more conductive to the CO_2RR into formate due to the moderate adsorption of $^*\text{OCHO}$ and the inhibition of HER.

3.4. Flow cell assessments

Furthermore, for confirming the advantages of laser processing, alloy electrode with channels fabricated by laser was directly used in flow cell. Different from traditional GDE, in this work, the $\text{Cu}_6\text{Sn}_5\text{/Sn}$ GDE as the working electrode was tried to directly used as GDL and catalyst without adhesives (Fig. 5a). To ensure that CO_2 could be pressed into the cathode compartment to form three-phase interfaces, the outlet of gas compartment was sealed, the actual demonstration diagrams were shown in Fig. S14. The intrinsic permeability of $\text{Cu}_6\text{Sn}_5\text{/Sn}$ GDE was measured to be $2.24 \times 10^{-16} \text{ m}^2$ (permeability calculation method could be found in Supporting Information) [50,51]. Fig. 5b showed FESEM images of the channels with the radius size of $\sim 20 \mu\text{m}$. The cross section of channel proved that there were channels for CO_2 to pass through, and the corresponding mapping images showed Sn worked as electrode and

GDL, meanwhile, Cu and Sn elements were uniformly distributed on surface of Sn foil (Fig. 5c and d).

To illustrate the effectiveness of flow cell and home-made GDE, the cathodic polarization curve of flow cell was tested. (Fig. 5e) Clearly, after adopting flow cell, the current density of $\text{Cu}_6\text{Sn}_5\text{/Sn}$ electrode reached over 100 mA cm^{-2} at -0.95 V vs. RHE. As shown in Fig. 5f and S15, at the optimized CO_2 flow rate of 30 sccm (Fig. S16), the $\text{Cu}_6\text{Sn}_5\text{/Sn}$ GDE exhibited high FE for CO_2RR to formate in the whole voltage range from -0.8 to -1.1 V vs. RHE, with the highest $\text{FE}_{\text{formate}}$ value of $\sim 86.69\%$ at -1.0 V vs. RHE. The activity of $\text{Cu}_6\text{Sn}_5\text{/Sn}$ GDE was compared with other GDE-based catalysts reported in recent years, as shown in Table S4, proving the successful application of home-made GDE in flow cell. Moreover, the long-term stability of $\text{Cu}_6\text{Sn}_5\text{/Sn}$ GDE was examined at the optimal overpotential. To avoid the influence of pH change on voltage and selectivity, the pH value was measured during the long-time stability test (Fig. S17). The current density and $\text{FE}_{\text{formate}}$ of $\text{Cu}_6\text{Sn}_5\text{/Sn}$ GDE in flow cell varied within a certain range at -1.0 V vs. RHE during continuous test for 24 h (Fig. 5g), and there were no evident changes occurred in the LSV curve after long-term test (Fig. S18), indicating the excellent stability of this system.

3.5. Finite element modelling analysis to CO_2RR performance on $\text{Cu}_6\text{Sn}_5\text{/Sn}$ GDE

X-ray CT was adopted to further verify the overall structure of $\text{Cu}_6\text{Sn}_5\text{/Sn}$ GDE, which laid a foundation for further modeling. Because

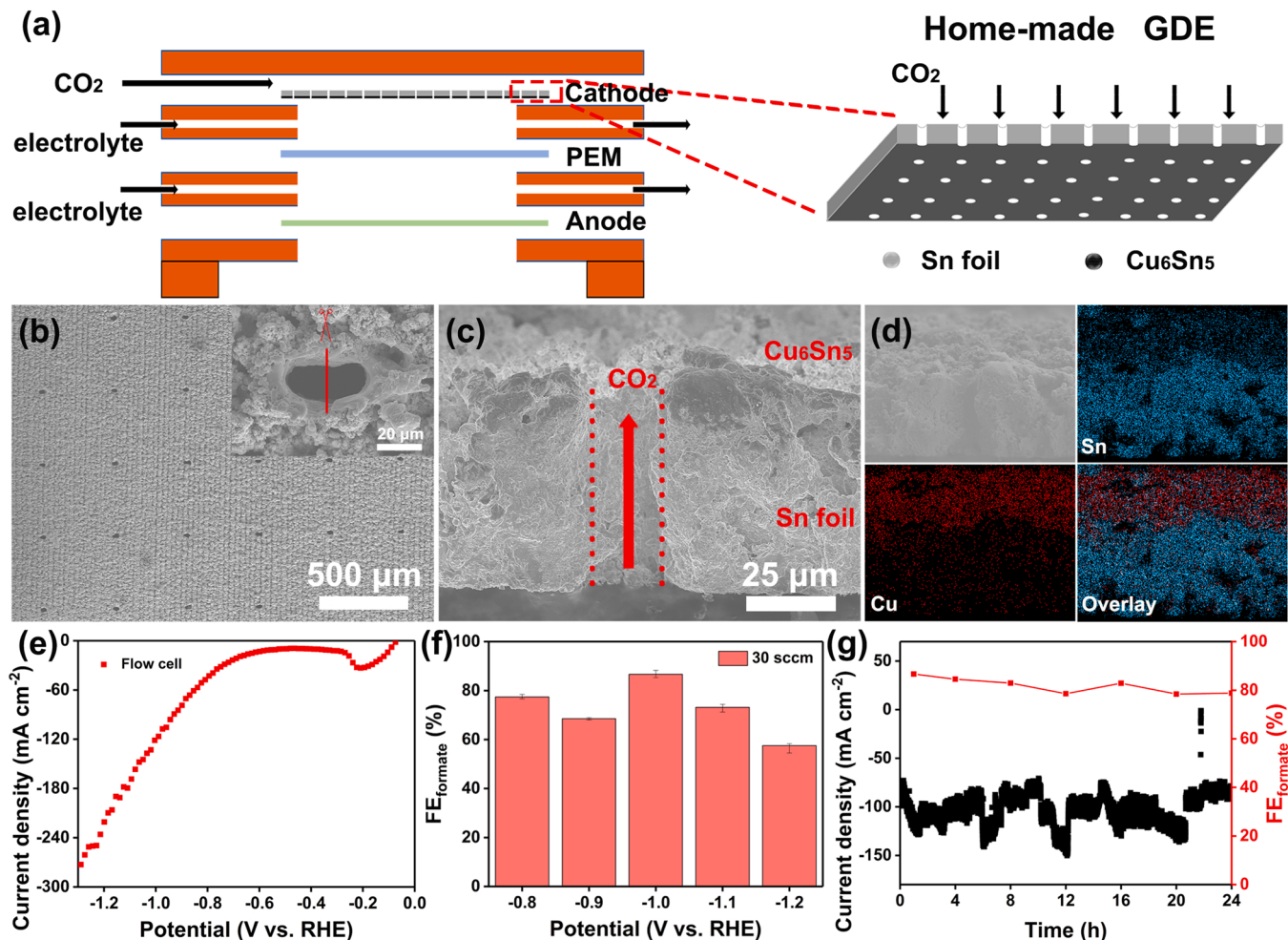


Fig. 5. (a) Schematic diagram of flow cell and home-made GDE. (b) SEM images of large size $\text{Cu}_6\text{Sn}_5\text{/Sn}$ GDE (insert: the image of single pore). The cross section of channel (c) and corresponding mapping results (d). (e) Polarization curve of $\text{Cu}_6\text{Sn}_5\text{/Sn}$ GDE in flow cell. (f) $\text{FE}_{\text{formate}}$ of $\text{Cu}_6\text{Sn}_5\text{/Sn}$ GDE at CO_2 flow rate of 30 sccm. (g) Long-term stability and $\text{FE}_{\text{formate}}$ curve of $\text{Cu}_6\text{Sn}_5\text{/Sn}$ GDE for 24 h at -1.0 V vs. RHE.

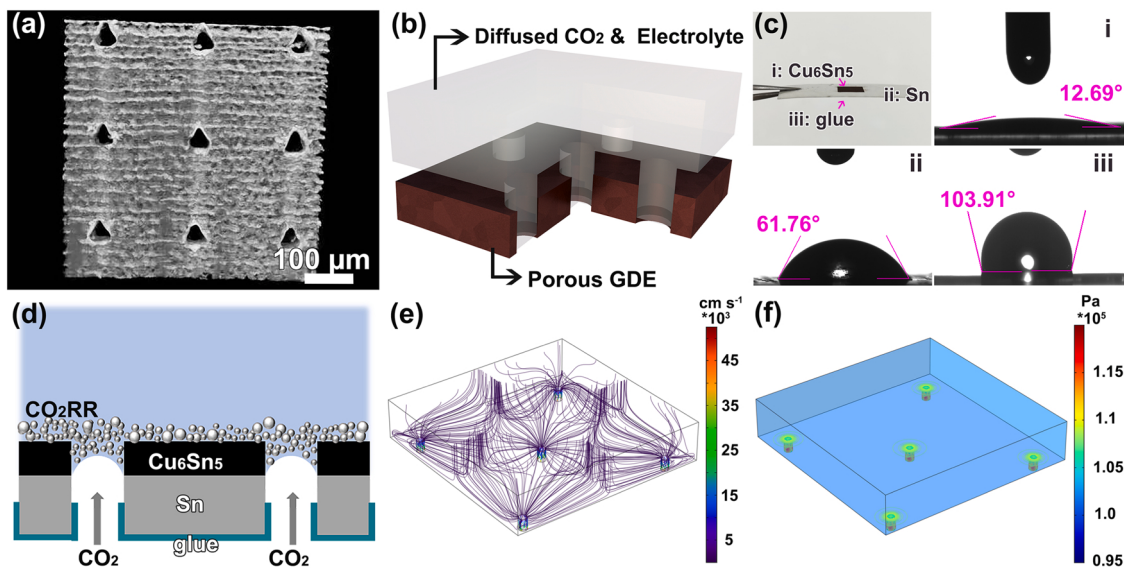


Fig. 6. (a) X-ray CT image of Cu₆Sn₅/Sn GDE. (b) Schematic diagram of porous GDE, diffused CO₂ and electrolyte. (c) Photograph and contact angles of (i) Cu₆Sn₅, channeled Sn substrate (ii) without and (iii) with glue. (d) Schematic of the liquid-gas interface advancing outside the channels, electrochemical CO₂RR occurred at the three-phase interface, where the electrocatalyst (solid), CO₂ (gas) and electrolyte (liquid) coexist. Simulation results of the velocity (e) and pressure field (f) of diffused CO₂ in the 3D model established by COMSOL Multiphysics.

the pore size and spacing used in the CO₂RR test were too small, the results of CT were not obvious, as shown in Fig. S19. In order to clearly show the overall structure of the channeled electrode, the channeled electrode with larger pore diameter (50 μm) and smaller spacing (200 μm) were prepared by utilizing the controllability of laser. The CT image in Fig. 6a and S20 indicated that the overall structures were

composed of Sn substrate as electron conduction layer, alloy catalyst layer with a characteristic rough morphology and CO₂ gas diffusion channels. According to the X-ray CT result, a 3D model was built to simulate the compose of porous GDE, diffused CO₂ and electrolyte in the flow cell (Fig. 6b). Besides, as shown in Fig. 6c and S21, Cu₆Sn₅ alloy showed a small contact angle, indicated a good wettability, while the

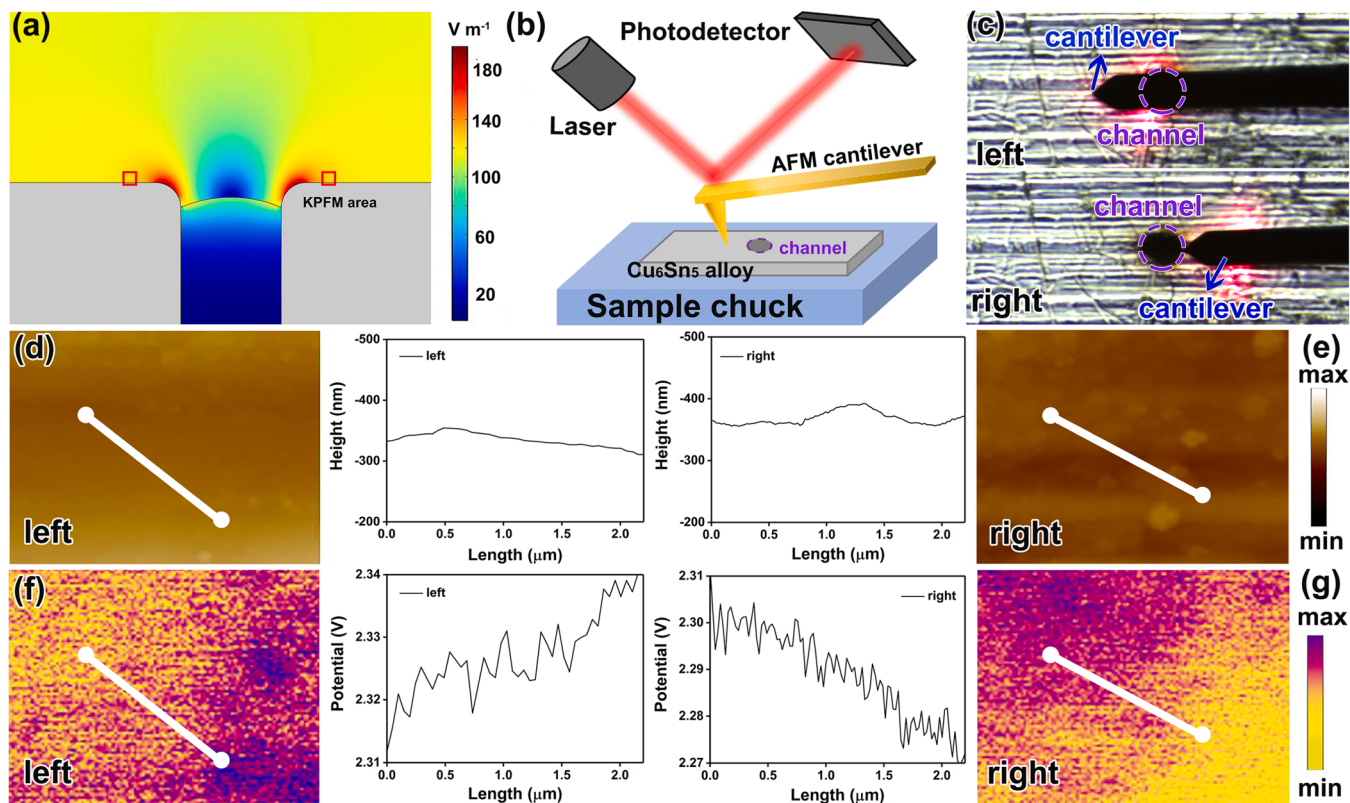


Fig. 7. (a) Simulation results of electric field distribution of diffused electrolyte in a 2D model. (b) Technical diagram of KPFM. (c) The selected positions on the left and right side of the channel. AFM images and corresponding surface height distribution curves of (d) the left and (e) right side. KPFM images tested under the applied voltage and corresponding surface potential distribution curve of (f) the left and (g) right side.

glue-treated Sn substrate was hydrophobic. Fig. 6d showed the liquid-gas interface advancing outside the channels. Limited by the pressure difference between liquid and gas compartment, the liquid-gas interface was pinned at the channel entrance and the interface curve was oriented towards the liquid. Further, the good wettability of Cu₆Sn₅ alloy provided a microenvironment with more active sites for the formation of three-phase interfaces, where CO₂RR took place. On the other hand, the hydrophobicity of glue-treated Sn substrate could repel flooding.

As shown in Fig. 6e and f, a 3D model was used to simulate the CO₂ concentration on the porous electrode, which was linearly related to the CO₂RR rate [52]. The model created through COMSOL Multiphysics (Fig. S22) included two regions of diffusion channel structure and CO₂ diffusion layer. Except for the target channels in the middle, four adjacent probes were added to imitate the potential impact of neighboring channels. Simulation results of the velocity (Fig. 6e and S23) and pressure field (Fig. 6f and S24) of diffused CO₂ in the 3D model proved the pressure inside the channels was lower and the velocity was faster; as CO₂ diffusing around the channels, the pressure first reached the maximum value and then gradually decreased outward, which was in accordance with Bernoulli equation. Given the pressure was positively related to the CO₂ concentration [53], these results indicated that the CO₂ concentration around the channels was the highest, and maintained at a higher level on the entire electrode surface, where was considered be more benefitted to CO₂RR.

In addition, it was believed that the electric field distribution would influence the rate of chemical reaction [54,55]. Note that the electric field was distributed in the diffused electrolyte in contact with the electrode. As shown in Fig. 7a, the simulation results of electric field distribution around the channels reached the highest, and gradually decreased along the diffusion direction to about 120 V m⁻¹. This result was consistent with the lighting protection theory, which indicated that the electric field distribution was noticeably higher in areas of higher curvature [56]. Further, KPFM, which enabled the study of the potential diversity on the sample surface [57–59], was used to verify the calculated results of electric field distribution. The technical diagram of KPFM was shown in Fig. 7b. The left and right sides of the channel were selected for testing (Fig. 7c). In order to avoid the influence of excessive surface coarseness on electric field distribution, relatively flat positions were selected based on the results of AFM (Fig. 7d–e). As could be seen from the results of KPFM, the potential gradually increased as the position got closer to the channel (Fig. 7f–g), which were in accordance with the simulation results (KPFM test areas were marked in Fig. 7a). In general, the combination of KPFM images and the calculated results proved that CO₂RR was most suitable to occur on Cu₆Sn₅ alloy around the channels of Cu₆Sn₅/Sn GDE. The Cu₆Sn₅/Sn with surface undulation showed the higher potential around the channel (Fig. S25).

4. Conclusions

In summary, we provided a strategy to fabricate the Cu₆Sn₅ alloy on Sn foil to obtain three-dimension electrode by one-step laser irradiation method. The Cu₆Sn₅ alloy enabled CO₂ reduction to formate with high FE (above 80% within a wide potential window), achieved maximum FE_{formate} of 87.2% at -0.95 V vs. RHE with a considerable formate partial current density of 28.69 mA cm⁻² and remarkable long-term stability (> 14 h) in 0.5 M NaHCO₃. DFT revealed the excellent catalytic performance benefited from the weakening of the binding energy of intermediates *OCHO and the suppression of the competitive HER. Furthermore, channeled Cu₆Sn₅/Sn electrode was directly used as multifunctional electrode for electrocatalysis and gas diffusion of CO₂, which showed the increased current density and high FE_{formate} (118 mA cm⁻² and 86.69% at -1.0 V vs. RHE). Experimental and simulation results of catalytic sites, CO₂ concentration and electric field distribution proved that CO₂RR was most suitable to occur on Cu₆Sn₅ alloy around the channels of Cu₆Sn₅/Sn GDE. These results highlighted the high efficiency of laser irradiation as a synthesis method and the

significant role of alloy and GDE on improving the CO₂RR performance for practical applications.

CRediT authorship contribution statement

Y.W. designed the systems, collected and analyzed data, and wrote the manuscript. Y.C., Y.Z., and J.Y. contributed to the analysis and discussion on the data. Z.L. performed the COMSOL Multiphysics simulation. Y.S. provided help and advice on the flow cell setup. H.L., X. L. and W.Z. supervised and guided the whole project.

Declaration of Competing Interest

The authors declare that they have no known competing financial interests or personal relationships that could have appeared to influence the work reported in this paper.

Acknowledgements

This work was supported by Taishan Scholars Project Special Funds (tsqn201812083), Natural Science Foundation of Shandong Province (ZR2019YQ20, 2019JMRH0410, ZR2020QE057), and the National Natural Science Foundation of China (51972147, 520222037, 52002145).

Appendix A. Supporting information

Supplementary data associated with this article can be found in the online version at doi:10.1016/j.apcatb.2021.120991.

References

- [1] S. Verma, S. Lu, P.J.A. Kenis, Co-electrolysis of CO₂ and glycerol as a pathway to carbon chemicals with improved technoeconomics due to low electricity consumption, *Nat. Energy* 4 (2019) 466–474, <https://doi.org/10.1038/s41560-019-0374-6>.
- [2] Z.Q. Chen, T. Wang, B. Liu, D.F. Cheng, C.L. Hu, G. Zhang, W.J. Zhu, H.Y. Wang, Z. J. Zhao, J.L. Gong, Grain-boundary-rich copper for efficient solar-driven electrochemical CO₂ reduction to ethylene and ethanol, *J. Am. Chem. Soc.* 142 (2020) 6878–6883, <https://doi.org/10.1021/jacs.0c00971>.
- [3] S. Nitopi, E. Bertheussen, S.B. Scott, X. Liu, A.K. Engstfeld, S. Horsch, B. Seger, I.E. L. Stephens, K. Chan, C. Hahn, J.K. Nørskov, T.F. Jaramillo, I. Chorkendorff, Progress and perspectives of electrochemical CO₂ reduction on copper in aqueous electrolyte, *Chem. Rev.* 119 (2019) 7610–7672, <https://doi.org/10.1021/acs.chemrev.8b00705>.
- [4] F. Lei, W. Liu, Y. Sun, J. Xu, K. Liu, L. Liang, T. Yao, B. Pan, S. Wei, Y. Xie, Metallic tin quantum sheets confined in graphene toward high-efficiency carbon dioxide electroreduction, *Nat. Commun.* 7 (2016) 1–8, <https://doi.org/10.1038/ncomms12697>.
- [5] T.C. Chou, C.C. Chang, H.L. Yu, W.Y. Yu, C.L. Dong, J.J. Velasco-Velez, C. H. Chuang, L.C. Chen, J.F. Lee, J.M. Chen, H.L. Wu, Controlling the oxidation state of the Cu electrode and reaction intermediates for electrochemical CO₂ reduction to ethylene, *J. Am. Chem. Soc.* 142 (2020) 2857–2867, <https://doi.org/10.1021/jacs.9b1126>.
- [6] M. Ebaid, K. Jiang, Z. Zhang, W.S. Drisdell, A.T. Bell, J.K. Cooper, Production of C₂/C₃ oxygenates from planar copper nitride-derived mesoporous copper via electrochemical reduction of CO₂, *Chem. Mater.* 32 (2020) 3304–3311, <https://doi.org/10.1021/acs.chemmater.0c00761>.
- [7] M. Zhu, L. Zhang, S. Liu, D. Wang, Y. Qin, Y. Chen, W. Dai, Y. Wang, Q. Xing, J. Zou, Degradation of 4-nitrophenol by electrocatalysis and advanced oxidation processes using Co₃O₄@C anode coupled with simultaneous CO₂ reduction via SnO₂/CC cathode, *Chin. Chem. Lett.* 31 (2020) 1961–1965, <https://doi.org/10.1016/j.ccl.2020.01.017>.
- [8] M. Zhang, Z. Zhang, Z. Zhao, H. Huang, D.H. Anjum, D. Wang, J. He, K.-W. Huang, Tunable selectivity for electrochemical CO₂ reduction by bimetallic Cu-Sn catalysts: elucidating the roles of Cu and Sn, *ACS Catal.* 11 (2021) 11103–11108, <https://doi.org/10.1021/acscatal.1c02556>.
- [9] D. Chen, Y. Wang, D. Liu, H. Liu, C. Qian, H. He, J. Yang, Surface composition dominates the electrocatalytic reduction of CO₂ on ultrafine CuPd nanoalloys, *Carbon Energy* 2 (2020) 443–451, <https://doi.org/10.1002/cey2.38>.
- [10] S.Y. Choi, S.K. Jeong, H.J. Kim, I.H. Baek, K.T. Park, Electrochemical reduction of carbon dioxide to formate on tin-lead alloys, *ACS Sustain. Chem. Eng.* 4 (2016) 1311–1318, <https://doi.org/10.1021/acssuschemeng.5b01336>.
- [11] Q. Yang, Q.L. Wu, Y. Liu, S.P. Luo, X.T. Wu, X.X. Zhao, H.Y. Zou, B.H. Long, W. Chen, Y.J. Liao, L.X. Li, P.K. Shen, L.L. Duan, Z.W. Quan, Novel Bi-doped amorphous SnO_x nanoshells for efficient electrochemical CO₂ reduction into

formate at low overpotentials, *Adv. Mater.* 32 (2020), 2002822, <https://doi.org/10.1002/adma.202002822>.

[12] Z. Tao, Z. Wu, Y. Wu, H. Wang, Activating copper for electrocatalytic CO_2 reduction to formate via molecular interactions, *ACS Catal.* 10 (2020) 9271–9275, <https://doi.org/10.1021/acscatal.0c02237>.

[13] W. Xiong, J. Yang, L. Shuai, Y. Hou, M. Qiu, X.Y. Li, M.K.H. Leung, CuSn alloy nanoparticles on nitrogen-doped graphene for electrocatalytic CO_2 reduction, *ChemElectroChem* 6 (2019) 5951–5957, <https://doi.org/10.1002/celec.201901381>.

[14] T.T.H. Hoang, S. Verma, S. Ma, T.T. Fister, J. Timoshenko, A.I. Frenkel, P.J. A. Kenis, A.A. Gewirth, Nanoporous copper-silver alloys by additive-controlled electrodeposition for the selective electroreduction of CO_2 to ethylene and ethanol, *J. Am. Chem. Soc.* 140 (2018) 5791–5797, <https://doi.org/10.1021/jacs.8b01868>.

[15] Y. Zhou, R. Zhou, X. Zhu, N. Han, B. Song, T. Liu, G. Hu, Y. Li, J. Lu, Y. Li, Mesoporous PdAg nanospheres for stable electrochemical CO_2 reduction to formate, *Adv. Mater.* 32 (2020), 2000992, <https://doi.org/10.1002/adma.202000992>.

[16] K.D. Gilroy, A. Ruditskiy, H.C. Peng, D. Qin, Y. Xia, Bimetallic nanocrystals: syntheses, properties, and applications, *Chem. Rev.* 116 (2016) 10414–10472, <https://doi.org/10.1021/acs.chemrev.6b00211>.

[17] J.G. Wang, J.S. Zou, X. Hu, S.L. Ning, X.J. Wang, X.W. Kang, S.W. Chen, Heterostructured intermetallic CuSn catalysts: high performance towards the electrochemical reduction of CO_2 to formate, *J. Mater. Chem. A* 7 (2019) 27514–27521, <https://doi.org/10.1039/c9ta11140a>.

[18] E. Irtem, D. Arenas Esteban, M. Duarte, D. Choukroun, S. Lee, M. Ibáñez, S. Bals, T. Breugelmans, Ligand-mode directed selectivity in Cu-Ag core-shell based gas diffusion electrodes for CO_2 electroreduction, *ACS Catal.* 10 (2020) 13468–13478, <https://doi.org/10.1021/acscatal.0c03210>.

[19] N.T. Nesbitt, T. Burdyny, H. Simonson, D. Salvatore, D. Bohra, R. Kas, W.A. Smith, Liquid-solid boundaries dominate activity of CO_2 reduction on gas-diffusion electrodes, *ACS Catal.* 10 (2020) 14093–14106, <https://doi.org/10.1021/acscatal.0c03319>.

[20] L. Du, Y.Y. Shao, J.M. Sun, G.P. Yin, J. Liu, Y. Wang, Advanced catalyst supports for PEM fuel cell cathodes, *Nano Energy* 29 (2016) 314–322, <https://doi.org/10.1016/j.nanoen.2016.03.016>.

[21] J. Li, G. Chen, Y. Zhu, Z. Liang, A. Pei, C.L. Wu, H. Wang, H.R. Lee, K. Liu, S. Chu, Y. Cui, Efficient electrocatalytic CO_2 reduction on a three-phase interface, *Nat. Catal.* 1 (2018) 592–600, <https://doi.org/10.1038/s41929-018-0108-3>.

[22] C.T. Dinh, T. Burdyny, M.G. Kibria, A. Seifitokaldani, C.M. Gabardo, F.P.G. de Arquer, A. Kiani, J.P. Edwards, P. De Luna, O.S. Bushuyev, C.Q. Zou, R. Quintero-Bermudez, Y.J. Pang, D. Sinton, E.H. Sargent, CO_2 electroreduction to ethylene via hydroxide-mediated copper catalysis at an abrupt interface, *Science* 360 (2018) 783–787, <https://doi.org/10.1126/science.aas9100>.

[23] J. Lin, Z.W. Peng, Y.Y. Liu, F. Ruiz-Zepeda, R.Q. Ye, E.L.G. Samuel, M.J. Yacaman, B.I. Yakobson, J.M. Tour, Laser-induced porous graphene films from commercial polymers, *Nat. Commun.* 5 (2014) 5714, <https://doi.org/10.1038/ncomms6714>.

[24] H. Hu, Q. Li, L.Q. Li, X.L. Teng, Z.X. Feng, Y.L. Zhang, M.B. Wu, J.S. Qiu, Laser irradiation of electrode materials for energy storage and conversion, *Matter* 3 (2020) 95–126, <https://doi.org/10.1016/j.matt.2020.05.001>.

[25] Y.S. Wu, Z. Huang, H.Q. Jiang, C. Wang, Y. Zhou, W. Shen, H.L. Xu, H.X. Deng, Facile synthesis of uniform metal carbide nanoparticles from metal-organic frameworks by laser metallurgy, *ACS Appl. Mater. Interfaces* 11 (2019) 44573–44581, <https://doi.org/10.1021/acsami.9b13864>.

[26] T. Zhang, Y. Bai, Y.Q. Sun, L.F. Hang, X.Y. Li, D.L. Liu, X.J. Lyu, C.C. Li, W.P. Cai, Y. Li, Laser-irradiation induced synthesis of spongy Au/AgPt alloy nanospheres with high-index facets, rich grain boundaries and subtle lattice distortion for enhanced, *J. Mater. Chem. A* 6 (2018) 13735–13742, <https://doi.org/10.1039/c8ta04087g>.

[27] J.B. Park, S.H. Jeong, M.S. Jeong, J.Y. Kim, B.K. Cho, Synthesis of carbon-encapsulated magnetic nanoparticles by pulsed laser irradiation of solution, *Carbon* 46 (2008) 1369–1377, <https://doi.org/10.1016/j.carbon.2008.05.011>.

[28] R. Xu, Y. Xie, R. Li, J. Zhang, T. Zhou, Direct bonding of polymer and metal with an ultrahigh strength laser treatment and mechanical interlocking, *Adv. Eng. Mater.* 23 (2021) 2001288–2024051, <https://doi.org/10.1002/adem.202001288>.

[29] G. Kresse, J. Furthmüller, Efficient iterative schemes for ab initio total-energy calculations using a plane-wave basis set, *Phys. Rev. B* 54 (1996) 11169–11186, <https://doi.org/10.1103/physrevb.54.11169>.

[30] G. Kresse, D. Joubert, From ultrasoft pseudopotentials to the projector augmented-wave method, *Phys. Rev. B* 59 (1999) 1758–1775, <https://doi.org/10.1103/PhysRevB.59.1758>.

[31] P.E. Blöchl, Projector augmented-wave method, *Phys. Rev. B* 50 (1994) 17953–17979, <https://doi.org/10.1103/PhysRevB.50.17953>.

[32] A.A. Peterson, F. Abild-Pedersen, F. Studt, J. Rossmeisl, J.K. Nørskov, How copper catalyzes the electroreduction of carbon dioxide into hydrocarbon fuels, *Energy Environ. Sci.* 3 (2010) 1311–1315, <https://doi.org/10.1039/C0EE00071J>.

[33] K. Ye, Z.W. Zhou, J.Q. Shao, L. Lin, D.F. Gao, N. Ta, R. Si, G.X. Wang, X.H. Bao, In situ reconstruction of a hierarchical Sn-Cu/SnO_x core/shell catalyst for high-performance CO_2 electroreduction, *Angew. Chem. Int. Ed.* 59 (2020) 4814–4821, <https://doi.org/10.1002/anie.201916538>.

[34] Y. Zhao, C.Y. Wang, G.G. Wallace, Tin nanoparticles decorated copper oxide nanowires for selective electrochemical reduction of aqueous CO_2 to CO , *J. Mater. Chem. A* 4 (2016) 10710–10718, <https://doi.org/10.1039/c6ta04155h>.

[35] F. Zhang, E. Alhajji, Y.J. Lei, N. Kurra, H.N. Alshareef, Highly doped 3D graphene Na-ion battery anode by laser scribing polyimide films in nitrogen ambient, *Adv. Energy Mater.* 8 (2018), 1800353, <https://doi.org/10.1002/aenm.201800353>.

[36] Y.K. Chen, J.Y. Yu, J. Jia, F. Liu, Y.W. Zhang, G.W. Xiong, R.T. Zhang, R.Q. Yang, D.H. Sun, H. Liu, W.J. Zhou, Metallic Ni₃Mo₃N porous microrods with abundant catalytic sites as efficient electrocatalyst for large current density and superstability of hydrogen evolution reaction and water splitting, *Appl. Catal. B* 272 (2020), 118956, <https://doi.org/10.1016/j.apcatb.2020.118956>.

[37] Z. He, F. Mansfeld, Exploring the use of electrochemical impedance spectroscopy (EIS) in microbial fuel cell studies, *Energy Environ. Sci.* 2 (2009) 215–219, <https://doi.org/10.1039/B814914C>.

[38] H. Xu, C. Peng, Y. Yan, F. Dong, H. Sun, J. Yang, S. Zheng, “All-In-One” integrated ultrathin SnS₂@3D multichannel carbon matrix power high-area-capacity lithium battery anode, *Carbon Energy* 1 (2019) 276–288, <https://doi.org/10.1002/cyey.222>.

[39] M. Kuhn, T.K. Sham, Charge redistribution and electronic behavior in a series of Au-Cu alloys, *Phys. Rev. B* 49 (1994) 1647–1661, <https://doi.org/10.1103/PhysRevB.49.1647>.

[40] N. Han, M. Sun, Y. Zhou, J. Xu, C. Cheng, R. Zhou, L. Zhang, J. Luo, B. Huang, Y. Li, Alloyed palladium-silver nanowires enabling ultrastable carbon dioxide reduction to formate, *Adv. Mater.* 33 (2021), 2005821, <https://doi.org/10.1002/adma.202005821>.

[41] D. Wang, A.C. Miller, M.R. Notis, XPS study of the oxidation behavior of the Cu₃Sn intermetallic compound at low temperatures, *Surf. Interface Anal.* 24 (1996) 127–132, [https://doi.org/10.1002/\(SICI\)1096-9918\(199602\)24:2<127::AID-SIA110>3.0.CO;2-Z](https://doi.org/10.1002/(SICI)1096-9918(199602)24:2<127::AID-SIA110>3.0.CO;2-Z).

[42] X.X. Jiang, X.K. Wang, Z.J. Liu, Q.L. Wang, X. Xiao, H.P. Pan, M. Li, J.W. Wang, Y. Shao, Z.Q. Peng, Y. Shen, M.K. Wang, A highly selective tin-copper bimetallic electrocatalyst for the electrochemical reduction of aqueous CO_2 to formate, *Appl. Catal. B* 259 (2019), 118040, <https://doi.org/10.1016/j.apcatb.2019.118040>.

[43] J.P. Perdew, J.A. Chevary, S.H. Vosko, K.A. Jackson, M.R. Pederson, D.J. Singh, C. Fiolhais, Atoms, molecules, solids, and surfaces: applications of the generalized gradient approximation for exchange and correlation, *Phys. Rev. B* 46 (1992) 6671–6687, <https://doi.org/10.1103/PhysRevB.46.6671>.

[44] J.P. Perdew, Y. Wang, Accurate and simple analytic representation of the electron-gas correlation energy, *Phys. Rev. B* 45 (1992) 13244–13249, <https://doi.org/10.1103/PhysRevB.45.13244>.

[45] A. Vasileff, X. Zhi, C. Xu, L. Ge, Y. Jiao, Y. Zheng, S.-Z. Qiao, Selectivity control for electrochemical CO_2 reduction by charge redistribution on the surface of copper alloys, *ACS Catal.* 9 (2019) 9411–9417, <https://doi.org/10.1021/acscatal.9b02312>.

[46] K. Ye, A. Cao, J.Q. Shao, G. Wang, R. Si, N. Ta, J.P. Xiao, G.X. Wang, Synergy effects on Sn-Cu alloy catalyst for efficient CO_2 electroreduction to formate with high mass activity, *Sci. Bull.* 65 (2020) 711–719, <https://doi.org/10.1016/j.scib.2020.01.020>.

[47] J.S. Yoo, R. Christensen, T. Vegge, J.K. Nørskov, F. Studt, Theoretical insight into the trends that guide the electrochemical reduction of carbon dioxide to formic acid, *ChemSusChem* 9 (2016) 358–363, <https://doi.org/10.1002/cssc.201501197>.

[48] J.T. Feaster, C. Shi, E.R. Cave, T. Hatsukade, D.N. Abram, K.P. Kuhl, C. Hahn, J. K. Nørskov, T.F. Jaramillo, Understanding selectivity for the electrochemical reduction of carbon dioxide to formic acid and carbon monoxide on metal electrodes, *ACS Catal.* 7 (2017) 4822–4827, <https://doi.org/10.1021/acscatal.7b00687>.

[49] Z. Cai, Y. Wu, Z. Wu, L. Yin, Z. Weng, Y. Zhong, W. Xu, X. Sun, H. Wang, Unlocking bifunctional electrocatalytic activity for CO_2 reduction reaction by win-win metal-oxide cooperation, *ACS Energy Lett.* 3 (2018) 2816–2822, <https://doi.org/10.1021/acsenergylett.8b01767>.

[50] S. Whitaker, Flow in porous media III: deformable media, *Transp. Porous Media* 1 (1986) 127–154, <https://doi.org/10.1007/BF00714689>.

[51] W. Ju, F. Jiang, H. Ma, Z. Pan, Y.B. Zhao, F. Paganí, D. Rentsch, J. Wang, C. Battaglia, Electrocatalytic reduction of gaseous CO_2 to CO on Sn/Cu-nanofiber-based gas diffusion electrodes, *Adv. Energy Mater.* 9 (2019) 1–6, <https://doi.org/10.1002/aenm.201901514>.

[52] Y.Y. Birdja, E. Pérez-Gallent, M.C. Figueiredo, A.J. Göttle, F. Calle-Vallejo, M.T. M. Koper, Advances and challenges in understanding the electrocatalytic conversion of carbon dioxide to fuels, *Nat. Energy* 4 (2019) 732–745, <https://doi.org/10.1038/s41560-019-0450-y>.

[53] H. Wang, C. Wang, X. Wang, F. Sun, Effects of carbon concentration and gas pressure with hydrogen-rich gas chemistry on synthesis and characterizations of HFCVD diamond films on WC-Co substrates, *Surf. Coat. Technol.* 409 (2021), 126839, <https://doi.org/10.1016/j.surcoat.2021.126839>.

[54] A.C. Aragónès, N.L. Haworth, N. Darwish, S. Ciampi, N.J. Bloomfield, G. G. Wallace, I. Diez-Perez, M.L. Coote, Electrostatic catalysis of a Diels-Alder reaction, *Nature* 531 (2016) 88–91, <https://doi.org/10.1038/nature16989>.

[55] D. Li, L. Huang, Y. Tian, T. Liu, L. Zhen, Y. Feng, Facile synthesis of porous Cu-Sn alloy electrode with prior selectivity of formate in a wide potential range for CO_2

electrochemical reduction, *Appl. Catal. B* 292 (2021), 120119, <https://doi.org/10.1016/j.apcatb.2021.120119>.

[56] S.H. Wang, Y.X. Yin, T.T. Zuo, W. Dong, J.Y. Li, J.L. Shi, C.H. Zhang, N.W. Li, C. J. Li, Y.G. Guo, Stable Li metal anodes via regulating lithium plating/stripping in vertically aligned microchannels, *Adv. Mater.* 29 (2017), 1703729, <https://doi.org/10.1002/adma.201703729>.

[57] J. Zhu, F. Fan, R. Chen, H. An, Z. Feng, C. Li, Direct imaging of highly anisotropic photogenerated charge separations on different facets of a single BiVO_4 photocatalyst, *Angew. Chem. Int. Ed.* 54 (2015) 9111–9114, <https://doi.org/10.1002/anie.201504135>.

[58] S. Hudlet, M. Saint Jean, B. Roulet, J. Berger, C. Guthmann, Electrostatic forces between metallic tip and semiconductor surfaces, *J. Appl. Phys.* 77 (1995) 3308–3314, <https://doi.org/10.1063/1.358616>.

[59] Y. Hou, K. Wang, D. Yang, Y. Jiang, N. Yennawar, K. Wang, M. Sanghadasa, C. Wu, S. Priya, Enhanced performance and stability in DNA-perovskite heterostructure-based solar cells, *ACS Energy Lett.* 4 (2019) 2646–2655, <https://doi.org/10.1021/acsenergylett.9b01894>.